Multispectral Reconstruction From Reference Objects in the Scene

Nirit Nussbaum-Hoffer, Tomer Michaeli
Technion
Israel
niritnu@gmail.com, tomer.m@ee.technion.ac.il

Abstract

*Hyperspectral imaging methods typically require dedicated cameras with extra optical elements (prisms, fibers, lenslet arrays), thus making them expensive and cumbersome to deploy. In this paper we explore a drastically different hyperspectral imaging approach, which requires no special optical components and can thus be used with any conventional camera. The idea is to place a reference object with a known spectrum (*e.g.* a black mask) within the field of view and to exploit the chromatic dependence of the Point Spread Function (PSF), in order to solve for the spectra of all other parts of the scene. We prove mathematically that chromatic-dependent blur cues alone are insufficient for fully recovering the spectrum of each pixel, even if the locations of edges in the (sharp) image are precisely known. Yet, we show that knowing the spectra at some of the pixels fully resolves this inherent ambiguity. We present an algorithm for solving the spectrum-from-reference inverse problem and illustrate its effectiveness through simulations as well as in a simple real world experiment.*

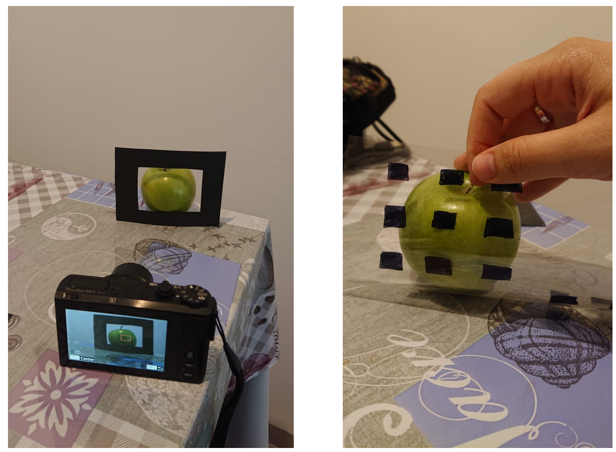

(a) Frame shaped mask (b) Grid shaped mask

Figure 1: **Multispectral imaging with an ordinary camera, using reference objects**. We show that placing a mask with a known spectrum (black in this case) within the field of view, is all that is needed in order to recover the spectral content of all objects in the scene. The mask can have, for example, the shape of a frame (left) or can be printed on a transparency and placed in front of the object (right).

1. Introduction

Hyperspectral imaging refers to the task of capturing an image at multiple (typically more than three) wavelength bands. This modality has numerous applications ranging from agriculture [4], to food processing [21] and geology [17] (see [8] for a comprehensive review). Existing hyperspectral imaging techniques either capture a sequence of 2D images, or rely on various priors to estimate the full hyperspectral cube from a single 2D image. However, despite the rapid progress over the last decades, all existing techniques involve dedicated cameras, which comprise special optical elements (*e.g.* prisms, fibers, lenslet arrays). This often makes them expensive and cumbersome.

In this paper, we explore a drastically different approach for hyperspectral imaging, which allows extracting spectral information from a single photograph captured by a conventional camera, with no additional optical elements. Our method exploits the fact that in any practical imaging system, the point spread function (PSF) is wavelength dependent, so that different spectral bands experience different blurs. This effect is particularly exacerbated, for example, when imaging slightly out-of-focus. This implies that the shape of the blur observed around edges in an image (even a grayscale one), carries information about the spectra of the objects in the scene. Unfortunately, we prove that this cue alone is insufficient for fully determining the spectra of the two scene elements residing on both sides of an edge. However, we show that when the spectrum on one side is known, the spectrum on the other side can be determined. Our approach thus relies on placing a reference object with a known spectrum within the field of view (*e.g.* a black mask), as illustrated in Fig. 1. This creates edges from which the spectra of all surrounding pixels can be resolved. The information can then be propagated to pixels farther away from the mask, until the spectra of all image pixels have been recovered.

We propose a simple algorithm for the spectrum-from-reference task, which uses the multi-channel Total Variation (TV) penalty to enforce that the edges in the recovered hyperspectral cube be aligned across different wavelength bands. We illustrate the method in the task of recovering multi-spectral images from grayscale measurements, both in simulations and in a simple real-world experiment.

1.1. Related Work

Most existing multispectral imaging methods can be broadly categorized into two families.

Scanning methods: These techniques construct a multispectral image from several 2D images. A classical example is the *push broom* technique, which uses a dispersive element to capture the spectral information of a 1D slice of an image and uses spatial scanning to stack many dispersed 1D slices into a 2D image with spectral information [11]. Another example is the *tunable filter* approach, in which several 2D images are captured sequentially, each with a different color filter. While simple, these techniques are limited in their ability to capture dynamic scenes [6][12].

Snapshot methods: In this family of solutions, only a single image is captured, and post-processing is used to estimate the entire hyperspectral cube. These methods are thus advantageous for dynamic scenes. The earliest snapshot imaging method is the *Integral Field Spectrograph* (IFS), which splits the image into several segments and reconstructs the spectral information of each independently [24, 25, 20, 16, 10, 13, 20, 7]. Other approaches apply different filters to different parts of the image [23, 19, 22]. In recent years, more involved snapshot imaging methods emerged, which are based on complex priors for estimating the hyperspectral information [9, 15, 14, 3, 1, 18]. While allowing shorter capture times than scanning methods, all existing snapshot methods also require dedicated optics.

2. The inherent ambiguity in blur cues

Our goal is to reconstruct k spectral bands $\{\bar{x}_i\}_{i=1}^k$ from a single grayscale image $\bar{y}$. Our key observation is that in any practical imaging system, different spectral bands experience different blurs. This can be due to diffraction limited blur (which is inherently wavelength dependent) or due to chromatic aberrations. This implies that the relation between $\{\bar{x}_i\}$ and $\bar{y}$ can be expressed as

$$\bar{y} = \sum_{i=1}^{k} \bar{h}_i * \bar{x}_i, \tag{1}$$

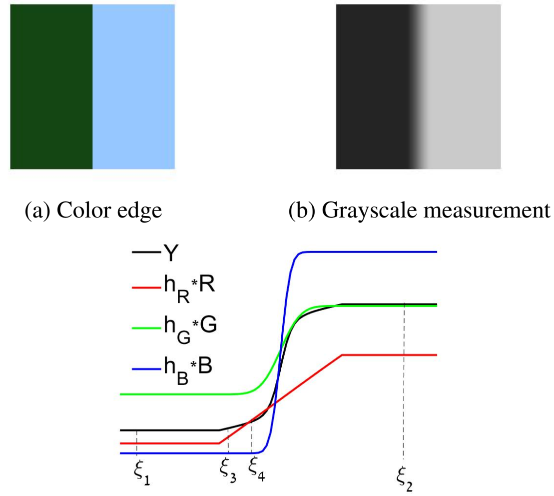

(a) Color edge (b) Grayscale measurement

(c) Horizontal cut

Figure 2: (a) A color edge scene comprising three color channels, $\bar{x}_1, \bar{x}_2, \bar{x}_3$. (b) The corresponding grayscale observation $\bar{y}$, is a result of convolving the channels with the PSFs $\bar{h}_1, \bar{h}_3, \bar{h}_3$, as described in (1). (c) A horizontal cut from (a) and (b).

where $\bar{h}_i$ is the PSF of the ith band and '$*$' denotes convolution. The implication of this observation is that the shape of the blur seen around edges in the grayscale image $\bar{y}$, encodes color information.

Unfortunately, these blur cues do not suffice for fully recovering the spectral bands. In fact, as we show next, it is impossible to reconstruct even a single edge (Fig. 2a) from its blurry graysclae version (Fig. 2b), without using some additional information.

Lemma 2.1. *Assume that the PSFs $\{\bar{h}_i\}_{i=1}^k$ are non-negative, integrate to* 1*, and have different supports, namely*

1. $\bar{h}_i(\xi) \geq 0, \quad \forall i,$
2. $\int \bar{h}_i(\xi) d\xi = 1, \quad \forall i,$
3. *supp*$\{\bar{h}_i\} \neq$ *supp*$\{\bar{h}_j\}, \quad \forall i \neq j.$

Consider a k-channel image of an edge taking the values $(q_1, \dots, q_k)$ on one side and $(r_1, \dots r_k)$ on the other side. Then it is possible to extract from the grayscale image $\bar{y}$ precisely $k+1$ independent equations in the $2k$ unknowns $\{(q_i, r_i)\}_{i=1}^k$. But any additional equation extracted from $\bar{y}$ will necessarily be dependent on the rest.

Proof. To simplify the exposition, let us start with the three-channel case, as illustrated in figures 2a and 2b. On the left side of the edge the color is (R_1, G_1, B_1), and on the right side the color is (R_2, G_2, B_2). Since the PSFs are non-negative and integrate to 1, the transition for each channel is monotonic (Fig. 2c), and each point along the grayscale edge has the form

$$\bar{y}(\xi) = \alpha R_1 + \beta G_1 + \gamma B_1 + \\ (1-\alpha)R_2 + (1-\beta)G_2 + (1-\gamma)B_2, \quad (2)$$

where $0 \leq \alpha, \beta, \gamma \leq 1$ depend on the location ξ along the edge. Since the PSFs have different supports, we can easily extract 4 independent equations (marked on Fig. 2c):

$$\bar{y}(\xi_1) = R_1 + G_1 + B_1, \quad (3)$$

$$\bar{y}(\xi_2) = R_2 + G_2 + B_2, \quad (4)$$

$$\bar{y}(\xi_3) = \alpha_1 R_1 + G_1 + B_1 + (1-\alpha_1)R_2, \quad (5)$$

$$\bar{y}(\xi_4) = \alpha_2 R_1 + \beta_2 G_1 + B_1 + (1-\alpha_2)R_2 + (1-\beta_2)G_2. \quad (6)$$

Equations (3) and (4) correspond to locations not affected by the PSF. Equations (5) and (6) correspond to locations where only one band is affected by the PSF and where only one band is not affected by the PSF, respectively (red and blue here, without loss of generality). We claim that any other observation (having the general form (2)) can be written as a linear combination of (3)-(6). To prove this, we write the coefficients of Eqs. (3)-(6) and (2) in a matrix

$$A = \begin{pmatrix} 1 & 1 & 1 & 0 & 0 & 0 \\ 0 & 0 & 0 & 1 & 1 & 1 \\ \alpha_1 & 1 & 1 & 1-\alpha_1 & 0 & 0 \\ \alpha_2 & \beta_2 & 1 & 1-\alpha_2 & 1-\beta_2 & 0 \\ \alpha & \beta & \gamma & 1-\alpha & 1-\beta & 1-\gamma \end{pmatrix}. \quad (7)$$

Now, clearly, the vectors

$$v_1 = \begin{pmatrix} -2 & 1 & 1 & -2 & 1 & 1 \end{pmatrix}^T,$$
$$v_2 = \begin{pmatrix} 1 & -2 & 1 & 1 & -2 & 1 \end{pmatrix}^T,$$
$$v_3 = \begin{pmatrix} 1 & 1 & -2 & 1 & 1 & -2 \end{pmatrix}^T,$$

are all in the null space of A. These vectors span a subspace of dimension 2 (v_1 and v_2 are linearly independent, but v_3 is a linear combination of v_1 and v_2). This implies that the null-space of A is at least of dimension 2. Therefore, $\text{Rank}(A) = 6 - \text{Nullity}(A) \leq 4$. However, since the first 4 rows of A are independent, we also have that $\text{Rank}(A) \geq 4$. These two facts imply that $\text{Rank}(A) = 4$, completing the proof for the three-channel setting.

In the general case of k channels, A has $2k$ columns and it is trivial to obtain $k+1$ independent equations as before. These constitute the first $k+1$ rows of A. Similarly, row $k+2$ corresponds to an arbitrary point along the edge. As before, we can find $k-1$ independent vectors in the null-space of A, among the k vectors

$$v_1 = \begin{pmatrix} -(k-1) & 1 & \dots & 1 & -(k-1) & 1 & \dots & 1 \end{pmatrix}^T$$
$$v_2 = \begin{pmatrix} 1 & -(k-1) & \dots & 1 & 1 & -(k-1) & \dots & 1 \end{pmatrix}^T$$
$$\vdots$$
$$v_k = \begin{pmatrix} 1 & 1 & \dots & -(k-1) & 1 & 1 & \dots & -(k-1) \end{pmatrix}^T$$

so that $\text{Nullity}(A) \geq k-1$. Therefore in this case, $\text{Rank}(A) = 2k - \text{Nullity}(A) \leq k+1$. Combining with the fact that $\text{Rank}(A) \geq k+1$, we get that $\text{Rank}(A) = k+1$, completing the proof for the general case. □

It is interesting to note that several hyperspectral imaging works did use chromatically dependent PSFs (usually via the introduction of a prism). Our lemma explains why these methods required additional modifications to the imaging process in order to resolve the inherent ambiguity. For example, [14] and [3] used a coded aperture. This resolves the ambiguity by creating artificial edges with a known color on one side (black). As we showed, the number of independent equations that can be extracted from the grayscale measurement of each such edge is $k+1$, which suffices for recovering the k unknown spectral bands on the other side.

Here we propose to use our insight in a different way, where instead of modifying the camera, we modify the scene. Specifically, we place a reference object within the field of view and use our knowledge of its spectrum to estimate the spectra of all other pixels in the image.

3. Algorithm

Let us start, for simplicity, with the case where the reference object is a black mask. We propose to estimate the spectral bands $\{\bar{x}_i\}_{i=1}^k$ of the scene from the grayscale image $\bar{y}$, by solving

$$\underset{x}{\text{argmin}} \frac{1}{2}\|Hx - y\|_2^2 + \beta \text{TV}(x) + \frac{\alpha}{2}\|Dx\|_2^2. \quad (8)$$

Here, y is a column vector representation of $\bar{y}$, x is a column vector representation of the channels $\{\bar{x}_i\}$ (concatenated one after the other), H is a matrix representing convolution with the PSFs $\{\bar{h}_i\}$ and summation, and D is a diagonal matrix containing 1's in the diagonal entries corresponding to mask pixels and 0's otherwise. Note that the dimension of x is k times larger than the dimension of y. The first term in (8) promotes solutions that are consistent with the measurements. The second term is the multichannel total variation (TV) regularizer, defined as

$$\text{TV}(x) = \int \sqrt{\sum_{k=1}^{K} \|\nabla \bar{x}_k(\xi)\|^2}\, d\xi \quad (9)$$

Algorithm 1 The spectrum-from-reference algorithm

1: set $k=0$, choose $\mu \geq 0$ and v_0, d_0
2: **repeat**
3: $\quad x_{k+1} \leftarrow \operatorname{argmin}_x \ \|Hx-y\|_2^2 + \mu\|x - v_k - d_k\|_2^2$ (Eq. (12))
4: $\quad v_{k+1} \leftarrow \operatorname{argmin}_v \ \beta \mathrm{TV}(v) + \frac{\alpha}{2}\|Dv\|_2^2 + \frac{\mu}{2}\|x_{k+1} - v - d_k\|_2^2$ (Eqs. (15),(16))
5: $\quad d_{k+1} = d_k + x_{k+1} - v_{k+1}$
6: $\quad k \leftarrow k+1$
7: **until** stopping criterion is satisfied

(we use a sum in place of the integral and approximate the gradient using discrete-space derivatives). This term promotes piece-wise smooth solutions, where edges in the different channels appear at the same locations. The third term encodes our prior about the color of the reference object, by promoting solutions where the pixels at the mask locations have values close to 0 (black). The constants β and α control the balance between the three terms.

We solve (8) using the ADMM algorithm. Specifically, we can rephrase (8) as

$$\begin{aligned} &\operatorname*{argmin}_{x,v} \frac{1}{2}\|Hx-y\|_2^2 + \beta \mathrm{TV}(v) + \frac{\alpha}{2}\|Dv\|_2^2 \\ &\text{s.t.} \qquad x = v. \end{aligned} \tag{10}$$

The corresponding augmented Lagrangian optimization problem is given by

$$\begin{aligned} \operatorname*{argmin}_{x,v} \frac{1}{2}\|Hx-y\|_2^2 + \beta \mathrm{TV}(v) + \frac{\alpha}{2}\|Dv\|_2^2 \\ + \frac{\mu}{2}\|x - v - d\|^2. \end{aligned} \tag{11}$$

Thus, applying the ADMM method, we obtain the spectrum-from-reference algorithm outlined in Alg. 1.

x-update The optimization problem in line 3 is a quadratic program, which possesses a closed form solution,

$$x_{k+1} = \left(H^T H + \mu I\right)^{-1}\left(H^T y + \mu(v_k + d_k)\right). \tag{12}$$

This solution can be implemented efficiently in the Fourier domain by noting that the matrix $H^T H$ involves k^2 convolution operations, which correspond to point-wise products in the frequency domain.

v-update In order to solve the optimization problem in line 4, we rearrange the equation to obtain a standard denoising problem. Specifically, denoting $f = x_{k+1} - d_k$ and dividing by $\frac{\mu}{2}$, line 4 can be written as

$$\begin{aligned} &\operatorname*{argmin}_{v} \frac{2\beta}{\mu}\mathrm{TV}(v) + \frac{\alpha}{\mu}\|Dv\|^2 + \|v - f\|^2 = \\ &\operatorname*{argmin}_{v} \frac{2\beta}{\mu}\mathrm{TV}(v) + v^T\left(\frac{\alpha}{\mu}D^T D + I\right)v - 2v^T f, \end{aligned} \tag{13}$$

where we subtracted the term $f^T f$, which does not depend on v. Now, defining

$$A = \left(\frac{\alpha}{\mu}D^T D + I\right)^{\frac{1}{2}}, \quad b = A^{-2}f, \quad \gamma = \frac{2\beta}{\mu}, \tag{14}$$

we can further simplify the objective as

$$\begin{aligned} &\operatorname*{argmin}_{v} \gamma \mathrm{TV}(v) + v^T A^T A v - 2v^T A^T A b = \\ &\operatorname*{argmin}_{v} \gamma \mathrm{TV}(v) + \|A(v-b)\|^2, \end{aligned} \tag{15}$$

where we used the fact that A is diagonal and added the term $\|Ab\|^2$, which does not depend on v. Note that the values on the main diagonal of A^2 are $1 + \frac{\alpha}{\mu}$ at locations associated with the black mask pixels, and 1 at the other locations. Therefore, this optimization problem can be interpreted as a conventional TV-denoising of b, but with a spatially varying regularization coefficient

$$\beta(\xi) = \gamma - \gamma\frac{\alpha}{\mu + \alpha}\bar{d}(\xi), \tag{16}$$

where $\bar{d}(\xi)$ is the binary mask. We solve this problem using Chambolle's algorithm [5].

Extending the algorithm to the case where the mask pixels are not necessarily black, is trivial. This can be done by modifying the objective to

$$\frac{1}{2}\|Hx-y\|^2 + \lambda \mathrm{TV}(x) + \frac{\alpha}{2}\|Dx - l\|^2 \tag{17}$$

where l is a vector containing the color values at the mask pixels. In this case the the algorithm remains the same, except that b of (14) is replaced by

$$b = A^{-2}\left(\frac{\alpha}{\mu}D^T l + f\right). \tag{18}$$

4. Simulations

We now illustrate the spectrum-from-reference algorithm in simulations. Algorithm 1 can accept any mask pattern and any PSF shape. We experiment with two types of mask patterns, as illustrated in Fig. 1: (i) a grid of black

(a) Out-of-focus PSF (b) Prism PSF

Figure 3: Simulated PSFs.

squares, and (ii) a black frame. We also experiment with two types of PSFs, as illustrated in Fig. 3: (i) an out-of-focus PSF, and (ii) a prism PSF. The out-of-focus PSF models a camera with a circular aperture, for which the PSF for wavelength λ is given by the Airy disk function

$$\bar{h}_\lambda(\xi) \propto \left(\frac{J_1\left(\frac{c\|\xi\|}{\lambda}\right)}{\frac{c\|\xi\|}{\lambda}} \right)^2. \tag{19}$$

Here $J_1(\cdot)$ is the Bessel function of the first kind and c is a constant that depends on the numerical aperture. As can be seen, in this case different wavelengths experience different blurs. This model is particularly relevant for situations where it is desired to use no additional optical elements besides a conventional camera (imaging out of focus). The prism PSF corresponds to placing a dispersive prism in between the object and the camera, right next to the object. For small incident angles and a small apex angle, the PSF is approximately a shifted delta function, where the shift for wavelength λ is proportional to the corresponding refractive index, n_λ. For simplicity, we assume that n_λ is a linear (decreasing) function over the range of wavelengths of interest, an approximation which is often quite reasonable. For both the out-of-focus PSF and the prism PSF, to obtain the PSF for channel i, we integrate over the range of wavelengths, $\mathcal{S}_i$, corresponding to that channel, so that

$$\bar{h}_i(\xi) = \int_{\mathcal{S}_i} \bar{h}_\lambda(\xi)\, d\lambda. \tag{20}$$

Figure 4 illustrates three-channel color image reconstruction with a grid mask and an out-of-focus PSF. In this simulation, we took a color image (Fig. 4a), multiplied it by a black mask (Fig. 4b), convolved each channel with its corresponding PSF, and summed the channels to obtain a simulated grayscale image (Fig. 4c). The algorithm receives the PSFs, the mask, and the blurred image as inputs, and outputs a reconstructed color image (Fig. 4d). Optionally, we can also perform inpainting with the multi-channel TV prior in order to fill-in the pixels obscured by the mask (Fig. 4e). Figure 5 shows an example color image reconstruction using the prism PSF. An example reconstruction

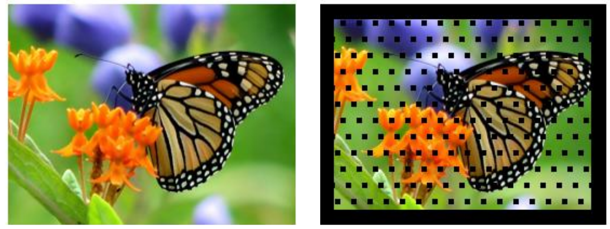

(a) Original image (b) Black mask

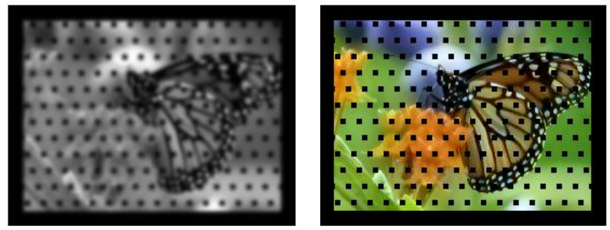

(c) Grayscale input (d) Reconstructed output

(e) Inpainted (optional output)

Figure 4: Three channel color reconstruction from a grayscale image captured out of focus (Airy disk PSF).

obtained with a colored mask can be seen in Fig. 6. Here we took the mask's colors to be precisely the colors of the scene at the corresponding pixels.

The effect of the number of spectral bands One of the strengths of the spectrum-from-reference method, is the flexibility in the number of wavelengths one can reconstruct. It must be noted, however, that increasing the number of reconstructed bands can adversely affect the quality of the reconstruction. This is because at a constant level of maximal out-of-focus blur (for the longest wavelength), the more channels we recover, the smaller the differences between their PSFs. Table 1 reports the root mean squared error (RMSE) obtained in reconstructing the same scene (Fig. 7a), each time with a different number of color channels. Here, we used the dataset of [2], which contains images with 31 color channels, and averaged over the spectral dimension when simulating less than 31 channels.

The effect of the mask's density The algorithm's performance is affected by the density of the mask's black regions. If too many black pixels are used, a lot of information is

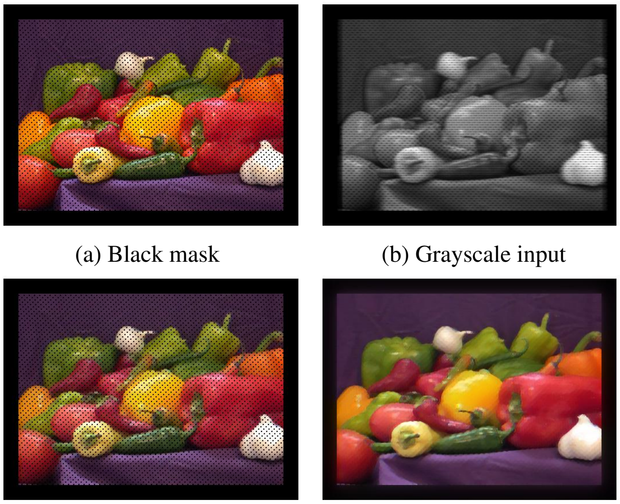

(a) Black mask (b) Grayscale input

(c) Reconstructed output (d) Inpainted output

Figure 5: Three channel color reconstruction from a grayscale image captured through a prism.

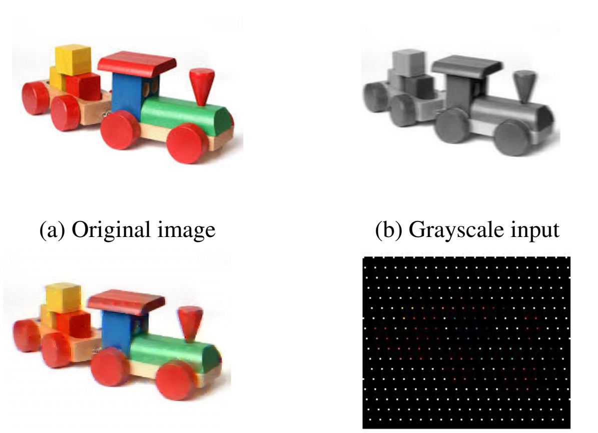

(a) Original image (b) Grayscale input

(c) Reconstruction (d) Mask with known colors

Figure 6: Color reconstruction with color constraints at the mask locations.

Number of channels	RMSE
3	7.652
8	11.51
16	12.47
31	12.69

Table 1: RMSE as a function of the number of reconstructed color channels using the out of focus PSF

lost. Yet, if too little black pixels are used, the colors reconstructed nearby the artificial edges need to propagate to larger distances, and thus the performance of the algorithm deteriorates. We found that the optimal gap (in terms of

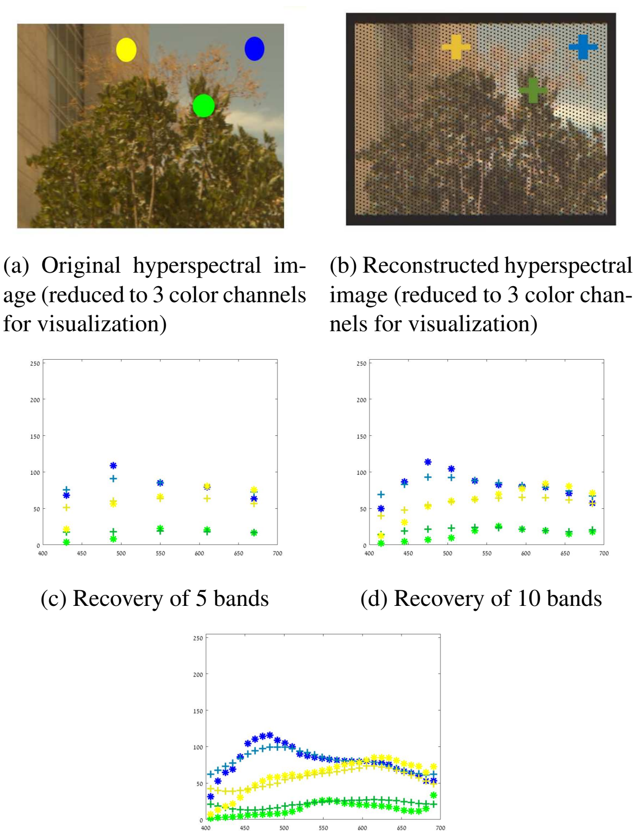

(a) Original hyperspectral image (reduced to 3 color channels for visualization)

(b) Reconstructed hyperspectral image (reduced to 3 color channels for visualization)

(c) Recovery of 5 bands

(d) Recovery of 10 bands

(e) Recovery of 31 bands

Figure 7: Hyperspectral image reconstruction. (c)-(e) The values of the original (circles) and the reconstructed (crosses) images at the three locations marked in (a),(b).

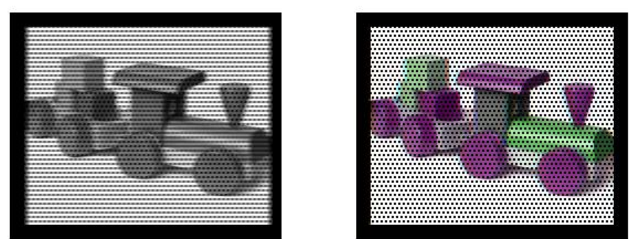

(a) Grayscale input (b) Reconstructed output

Figure 8: Three channel color image reconstruction with a prism PSF whose support is greater than the gap between adjacent black mask rectangles.

MSE for the non-black pixels) between two adjacent mask rectangles is precisely the total support length of the PSFs. Taking a smaller gap has a dramatic effect on the results, as illustrated in Fig. 8. Taking a larger gap, on the other hand, results in only a mild degradation and has the advantage of blocking less light.

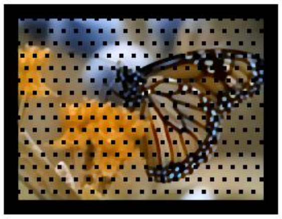

(a) Input PSNR = ∞

(b) Input PSNR = 49.49

(c) Input PSNR = 39.56

Figure 9: Color reconstruction from a noisy grayscale image using a large regularization parameter β.

The effect of noise Real world measurements are contaminated by noise, whose effect can be partly mitigated by increasing the regularization parameter β in (8). Yet this comes at the cost of less accurate reconstructed colors. Figure 9 illustrates this by depicting reconstructions from three different noisy grayscale versions of the same scene. In all cases, we used Poisson noise and optimally tuned the regularization parameter β for an input PSNR of 50dB. As can be seen, for PSNR ≥ 50, the noise is suppressed but the reconstructed colors are inaccurate, whereas for PSNR < 50 the noise is not sufficiently suppressed. This experiment shows that reconstruction with the out-of-focus PSF is relatively sensitive to noise, suggesting that the spectrum-from-reference method may be inappropriate for use in dim light or short exposure time conditions.

Effect of mask location inaccuracies In practice, determining the mask locations from the blurry grayscale image, cannot be done with infinite precision. It is therefore important to analyze how the algorithm performs when the mask it receives does not match the true one. The more conservative case, is where the algorithm receives a mask that is fully contained in the real one, as illustrated in Fig. 10b. In this case, the reconstruction almost does not change with respect to the case where the mask is known precisely (Fig. 10c). This is because the black mask pixels of which the algorithm was not informed, are simply treated as unknown colors, and are faithfully reconstructed just like the rest of the image. However, when the algorithm receives a wrong mask that contain non-mask regions (Fig. 10d), the results severely deteriorate as the algorithm attempts to enforce black regions where there ought to be color (Fig. 10e).

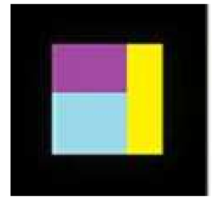

(a) Original image

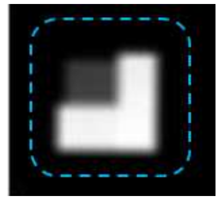

(b) Conservative mask

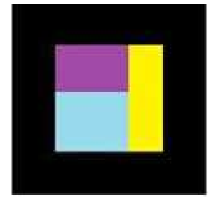

(c) Recovery with conservative mask

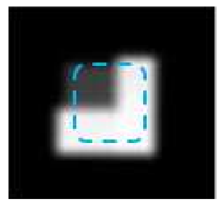

(d) Wrong mask

(e) Recovery with wrong mask

Figure 10: Effect of inaccurate knowledge of the mask.

5. A Proof-of-concept experiment

Figure 11 shows an experimental setup for exploring the use of spectrum-from-reference in a real imaging setting. Here, we used a conventional camera, from which we extracted the raw images. We took weighted averages of 2×2 blocks corresponding to the (R,G,G,B) Bayer pattern, in order to obtain a *grayscale* measurement. We displayed a color image on a screen and focused the camera on an object placed between the screen and the camera. This ensured the screen was out of focus. To measure the camera's PSFs in this setting, we first captured three images, with a single red/green/blue dot (Fig. 12). We used $\beta = 10^{-3}$ and applied white balance to the reconstructed colors, so that they can be compared with the true colors of the image displayed on the screen. The final reconstructed image is shown in Fig. 13.

Recall that theoretically, it is possible to recover colors from blur cues even if colors on both sides of an edge are mapped to the same gray values. In this case, had we captured the object in focus (*i.e.* without blur), the resulting grayscale image would contain no edge. But in the presence of (wavelength dependent) blur, the transition between the two colors becomes visible, and allows extracting the colors from the gray values. This phenomenon is illustrated

Figure 11: Experimental setup.

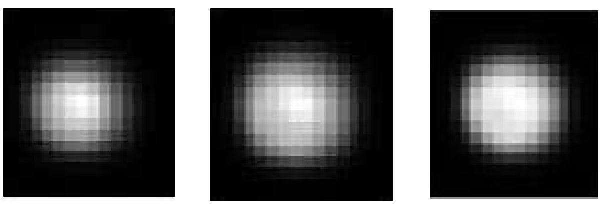

(a) Red channel (b) Green channel (c) Blue channel

Figure 12: Measured PSFs.

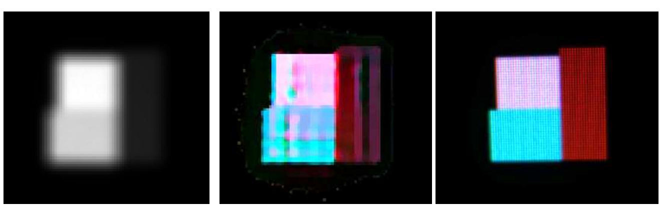

(a) Captured image (b) Reconstruction (c) Original colors

Figure 13: Experimental results.

in Fig. 14.

To test our ability to recover colors in such challenging conditions, we performed another experiment, as shown in Fig. 15. As can be seen, here the results are not as good, since the blur cues nearby the edges are very small and thus masked by the noise.

6. Conclusion and future directions

We explored a new approach for multispectral imaging, which uses a spectral reference object placed in the field of view, and exploits the chromatic dependence of the camera's PSF. We illustrated the method through simulations,

(a) Edge image (b) Grayscale measurement (c) Horizontal cut from (b)

Figure 14: (a) Color edge image. (b) Simulated blurry grayscale image. (c) Horizontal cut from (b). The transition between the two colors is apparent in (b), even though they have the same gray value.

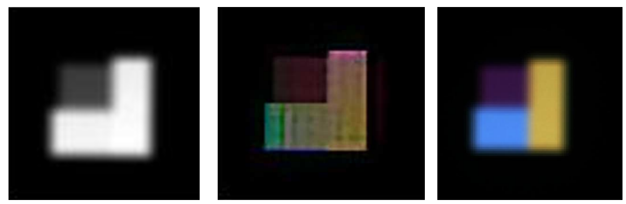

(a) Captured Image (b) Reconstruction (c) Original colors

Figure 15: Experimental reconstruction of colors having the same gray level.

as well as in a simple real-world experiment. One of the shortcomings of relying on conventional cameras, is that the dependence of their PSFs on the wavelength is relatively mild, thus making the reconstruction sensitive to noise. This fact can be partly overcome by using better priors in the reconstruction process. One particularly promising direction, seems to be the use of deep learning techniques for the reconstruction. Given that enough multispectral training data can be collected, this will allow obtaining better reconstructions than those obtained with the naive TV-prior.

Acknowledgement This research was supported by the Ollendorff Minerva Center of the Technion.

References

[1] Application of multiple-image fourier transform spectral imaging to measurement of fast phenomena. *Optical Review*, 1(2):205–207, 1994. 2

[2] B. Arad and O. Ben-Shahar. Sparse recovery of hyperspectral signal from natural rgb images. In *European Conference on Computer Vision*, pages 19–34. Springer, 2016. 5

[3] A. Bodkin, A. Sheinis, A. Norton, J. Daly, S. Beaven, and J. Weinheimer. Snapshot hyperspectral imaging: The hyperpixel array camera. *Proceedings of SPIE - The International Society for Optical Engineering*, 05 2009. 2, 3

[4] M. Borengasser, W. Hungate, and R. Watkins. *Hyperspectral Remote Sensing: Principles and Applications*. Remote Sensing Applications Series. CRC Press, 2007. 1

[5] A. Chambolle. An algorithm for total variation minimization and applications. *Journal of Mathematical imaging and vision*, 20(1-2):89–97, 2004. 4

[6] C.-I. Chang. *Hyperspectral data exploitation: theory and applications*. John Wiley & Sons, 2007. 2

[7] G. Courtes, Y. Georgelin, R. Bacon, M. G., and J. Boulesteix. A new device for faint objects high resolution imagery and bidimensional spectrography. *Instrumentation for Ground-Based Optical Astronomy. Santa Cruz Summer Workshops in Astronomy and Astrophysics*, 6302, 1988. 2

[8] A. Dacal-Nieto, A. Formella, P. Carrión, E. Vazquez-Fernandez, and M. Fernández-Delgado. Non–destructive detection of hollow heart in potatoes using hyperspectral imaging. In P. Real, D. Diaz-Pernil, H. Molina-Abril, A. Berciano, and W. Kropatsch, editors, *Computer Analysis of Images and Patterns*, pages 180–187, Berlin, Heidelberg, 2011. Springer Berlin Heidelberg. 1

[9] M. R. Descour, C. E. Volin, E. L. Dereniak, T. M. Gleeson, M. F. Hopkins, D. W. Wilson, and P. D. Maker. Demonstration of a computed-tomography imaging spectrometer using acomputer-generated hologram disperser. *Appl. Opt.*, 36(16):3694–3698, Jun 1997. 2

[10] D. Fletcher-Holmes and A. Harvey. Real-time imaging with a hyperspectral fovea. *J. Opt. A: Pure Appl. Opt*, 7:298–302, 06 2005. 2

[11] J. E. Fowler. Compressive pushbroom and whiskbroom sensing for hyperspectral remote-sensing imaging. In *2014 IEEE International Conference on Image Processing (ICIP)*, pages 684–688, Oct 2014. 2

[12] N. Gat. Imaging spectroscopy using tunable filters: a review. In *Wavelet Applications VII*, volume 4056, pages 50–64. International Society for Optics and Photonics, 2000. 2

[13] N. Gat, G. Scriven, J. Garman, M. De Li, and J. Zhang. Development of four-dimensional imaging spectrometers (4d-is). In *Imaging Spectrometry XI*, volume 6302, page 63020M. International Society for Optics and Photonics, 2006. 2

[14] M. E. Gehm, R. John, D. J. Brady, R. M. Willett, and T. J. Schulz. Single-shot compressive spectral imaging with a dual-disperser architecture. *Opt. Express*, 15(21):14013–14027, Oct 2007. 2, 3

[15] A. R. Harvey and D. W. Fletcher-Holmes. High-throughput snapshot spectral imaging in two dimensions. In *Spectral Imaging: Instrumentation, Applications, and Analysis II*, volume 4959, pages 46–54. International Society for Optics and Photonics, 2003. 2

[16] J. M. Hill, J. Angel, J. S. Scott, D. Lindley, and P. Hintzen. Multiple object spectroscopy-the medusa spectrograph. *The Astrophysical Journal*, 242:L69–L72, 1980. 2

[17] F. A. Kruse, J. W. Boardman, and J. F. Huntington. Comparison of airborne hyperspectral data and eo-1 hyperion for mineral mapping. *IEEE Transactions on Geoscience and Remote Sensing*, 41(6):1388–1400, June 2003. 1

[18] M. Kudenov and E. Dereniak. Compact real-time birefringent imaging spectrometer. *Optics express*, 20:17973–86, 07 2012. 2

[19] S. Mathews. Design and fabrication of a low-cost, multispectral imaging system. *Applied optics*, 47:F71–6, 11 2008. 2

[20] S. Morris and M. Dubbeldam. Microslices and low cost spectrographs for million element integral field spectroscopy. *Proceedings of SPIE - The International Society for Optical Engineering*, 4842, 02 2003. 2

[21] J. Qin, K. Chao, M. S. Kim, R. Lu, and T. F. Burks. Hyperspectral and multispectral imaging for evaluating food safety and quality. *Journal of Food Engineering*, 118(2):157–171, 2013. 1

[22] R. Shogenji, Y. Kitamura, K. Yamada, S. Miyatake, and J. Tanida. Multispectral imaging using compact compound optics. *Opt. Express*, 12(8):1643–1655, Apr 2004. 2

[23] B. A. Spiering. Multi spectral imaging system, May 1999. US Patent 5,900,942. 2

[24] J. H. Walraven, T. Walraven. Some features of the leiden radial velocity instrument. *Proceedings of ESO/CERN conference on auxiliary instrumentation for large telescopes*, pages 175–183, June 1972. 2

[25] Weitzel, L., Krabbe, A., Kroker, H., Thatte, N., Tacconi-Garman, L. E., Cameron, M., and Genzel, R. 3d: The next generation near-infrared imaging spectrometer. *Astron. Astrophys. Suppl. Ser.*, 119(3):531–546, 1996. 2